Chapter 4: Lattice Performance and Data Analysis

In this chapter we present details of the SBTE beam and diagnostics and of the analytical techniques used to interpret the data. We discuss diagnostic performance and calibration, particle energy calibration, background gas interaction with the beam, and how actual performance compared with the design parameters for the source. Errors are discussed in Ch. 7.

The SBTE was assembled in stages, with procedures and diagnostics changing from time to time as a result of measurements and growing experience. The source was installed first, and during its checkout we determined what size slit we should use for emittance measurements. As the lattice was gradually installed, we tested our Faraday cups, emittance measurement procedures, and beam tuning procedures, inproving each in the process. We found that we needed Faraday cups having no grids to intercept beam if we were to get absolute measurements of beam current, and that we needed to provide automated data collection and storage to improve the resolution of the phase space measurements and facilitate data analysis. When we found that we had not reached the low-emittance stability limit of current-dominated beam transport for $\sigma_0 < 90°$ with our initial beam parameters, we shortened the injector assembly to double its current output. Finally, we incorporated charge collectors with the downstream slits of our emittance measurement apparatus to increase the area in phase space accessible to measurement (the diagnostic acceptance). Although some data were taken during this process of change, almost all of the data reported below were taken after these changes were completed.

4.1 Injector Perveance and Performance

The "perveance" of a beam from a diode is the ratio $I/V^{\frac{3}{2}}$, where I is the current of the beam and V is the energy of the particles in eV. It is a

Device	Generalized perveance
SBTE	5.5×10^{-3}
proposed HTE	$< 2 \times 10^{-4}$
proposed driver	$1\text{--}5 \times 10^{-4}$

Table 4.1: Generalized perveances for SBTE and for two proposed accelerators

measure of the intensity of the space-charge forces in the beam. A related quantity, defined for a beam without regard to its source, is the dimensionless perveance found in the envelope equations of section 2.2.2, called the generalized perveance, Q. It is defined in the nonrelativistic limit by

$$Q = \frac{qI}{\zeta \pi \epsilon_0 m v_z^3} \quad \left(= \frac{1}{4\pi\epsilon_0} \sqrt{\frac{2m}{q}} \times \frac{I}{V^{\frac{3}{2}}} \right).$$

for conv

The space-charge forces of the SBTE beam are large compared to those of beams proposed for HIF use, as we show in Table 4.1. The SBTE beam is by this measure an order of magnitude more intense than the beam required to drive a HIF target. Even at the low-energy end of the HIF driver, where space-charge effects are most severe, the generalized perveance of each beam of the driver in some scenarios is lower than that of the SBTE beam. In a driver for HIF, the anticipated total number of ions is equivalent to about 300 μC of "particle" charge, and the final energy at the target will be about 10 GeV. For a 5-μsec-long pulse at the source, using 100 beams (for the initial period of acceleration, merging them into about 10–20 beams as the energy increases) [37], the current per beam is about 0.6 A. If the source energy can be made as high as 3 MV (it must be as high as technologically possible, because in low-velocity, low-current operation, an induction linac is very inefficient) then we have, for singly charged ions, that $Q \sim 2 \times 10^{-3}$.

We compare the values of the beam radius and divergence calculated by Dr. C. Kim [38] with the measured values as a function of current from the injector in Fig. 4.1. The beam parameters are varied by changing the voltages on the various electrodes while maintaining the output voltage at a constant value. The potential drop between the source and the first aperture plate controls the source current, and the variation of the accelerating field along the injector determines the focusing applied to the beam, and hence the optics of the beam at the injector exit. The difference between calculated and measured beam quantities can easily be explained by thermal expansion of the aperture plates, and the consequent alteration of the electrode spacing and accelerating gradient from the design values. In a bench test, we applied a hot air gun to the final aperture plate (the largest and most sensitive to thermal expansion effects) and we observed a 0.2-inch deflection of the final aperture to result from an approximately 50° C temperature change. This degree of motion of the plate would alter the final optics somewhat.

4.2 Particle Energy and Lattice Strength Calibration

The monitor chains for the quadrupole power supplies shown in Fig. 3.7 were well-calibrated. The error in measurement of the beam energy is the major source of uncertainty in the σ_0 calibration of the lattice. The Marx generator output, with an RC decay time of about 0.6 msec (0.15% per μsec droop) is coupled to the various gun electrodes through a capacitive divider. We used pulses with durations of about 10 μsec. The droop with time of the particle energy, and hence velocity, results in a slight debunching of the beam as it passes through the channel. The result for linear debunching is

$$\frac{1}{I}\frac{\partial I}{\partial z} = \frac{1}{2v_z}\frac{1}{V}\frac{\partial V}{\partial t},$$
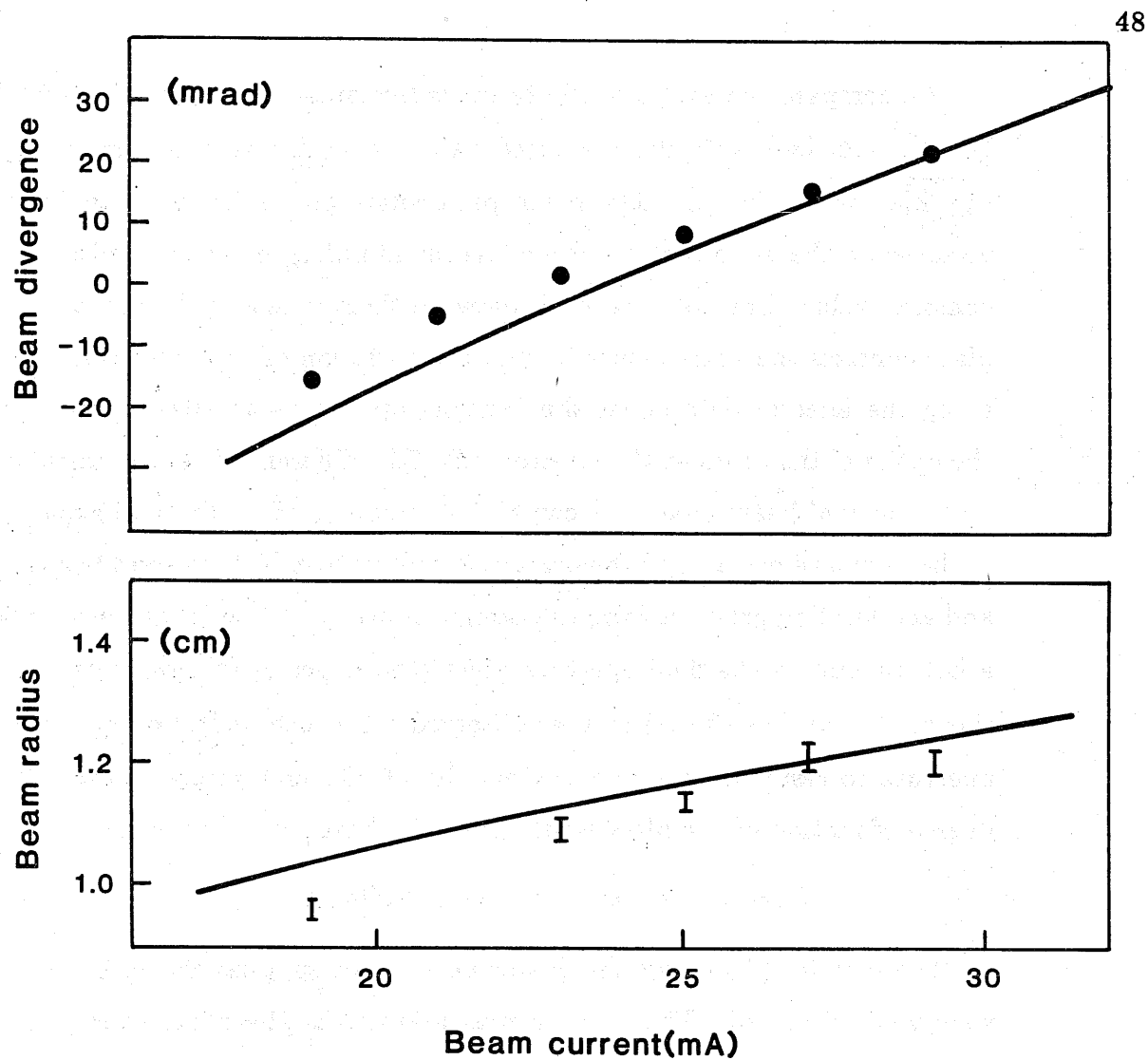
Figure 4.1: Comparison of measured and calculated injector output, with the initial injector design, operating at 160 kV. The agreement with the design values is good.

where I is the beam current, V is the beam energy, z is distance along the channel, and v_z is the velocity of the beam along the channel. The calculated current droop for 120 keV particle energy is only about 2.5% over the length of the channel ($\sim$ 13 meters). This energy variation also causes the beam centroid to move transversely with time within the channel. This is due to misalignments and the variation in focusing properties of the lenses with particle energy. This sweeping phenomenon from head to tail of the bunch was most noticeable at high lattice strengths, for which the misalignment effects give larger beam offsets.

We expect the calculation of the σ_0 values of the lattice as a function of particle energy and applied field to be very accurate. The major error is due to inexact measurement of the focusing field and particle energy. The calibration of the gun voltage was made with a capacitive divider, directly monitoring the source voltage through the Marx tank oil dielectric. A schematic diagram is included in the Marx schematic in Fig. 3.5. The divider ratio was measured at low-voltage to be 3182:1. The only components subject to high voltage stress were the metal and oil elements in the Marx tank. These were coupled to the 50 Ω cable which served as the large capacitor to ground in parallel with the oscilloscope. We know of no dielectric nonlinearity effects that could change the division ratio at the field strength in use.

All results presented here are based on the capacitive divider energy measurement, supported by results from a 90° electrostatic energy analyzer [39] and by time-of-flight measurements. The measurements reported here were made using 17.85±.03 kV as the charging potential on the Marx. The various energy determinations have errors of about ±1 kV. We obtained 122.5 keV from the divider, 123.0 keV from the energy analyzer, and 122.0 keV from the time-of-flight measurement.

We measured σ_0 by displacing a low-current beam and measuring the wavelength of the coherent oscillation as a function of the quadrupole voltage over the range $40° < \sigma_0 < 80°$. We used a beam current of 0.35 mA, for which image-charge effects were calculated to be negligible. The results are shown in Fig. 4.2 and Table 4.2. We measured the beam centroid as a function of strength of the lenses Q6–Q82 at four points along the lattice, just downstream from Q5, Q35, Q59, and Q79. As the lattice strength is varied, the initial phase of a beam injected with nonzero displacement will shift. We injected the beam at zero displacement to ensure that the initial phase of the betatron oscillation was zero ($\psi_0 = 0$, see Eqn. 2.3), giving the sine-like orbit for any lattice strength. The amplitude will grow smaller in a well-aligned lattice with increasing lattice strength, although the local offset in any one quadrupole may grow if misalignments cause the ideal orbit center to shift.

The results agree very well with calculations based on the measured beam energy over this range of σ_0, as shown in the table. We estimate that we have a $\pm 10°$ range of error in the phase determination at each measurement point, giving us the value of the accumulated phase change $\Delta\psi$ over the 37 periods from Q5 to Q79 to within about $\pm 20°$. This results in an uncertainty in the phase advance rate per period of about $\pm 0.6°$. Values of σ_0 greater than $80°$ were calculated from the applied lens voltage and measured particle energy.

4.3 Beam Matching Procedures

In order to calculate how to match the beam into the lattice, we need to know the initial x and y radius and divergence of the beam at the source. We could measure the horizontal properties much more accurately than the vertical properties. Because the beam did not depart from azimuthal symmetry enough to detect with our vertical resoution, we assumed this symmetry for

Centroid Position at Q79H vs. Quad Potential for Various x' Values, 0.35 mA
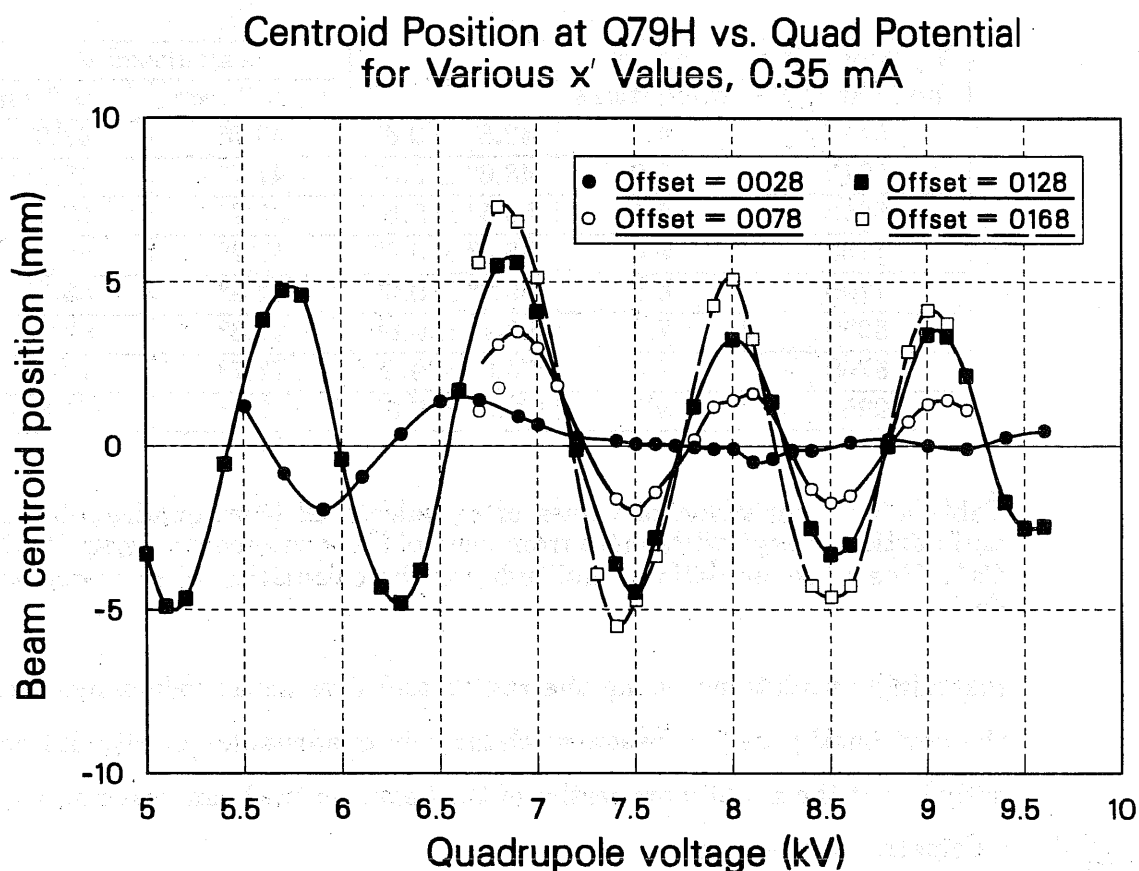
XCG 864-7156

Figure 4.2: Direct measurement of σ_0 in the lattice. We provided a node in the beam offset at Q5, and measured the accumulated phase advance for the motion of the beam centroid in the lattice for low current, as a function of lattice strength. Dividing the total phase advance by the number of intervening lattice periods gives σ_0. The limits on the range of the quadrupole voltage for each curve were set by the onset of beam loss, which would alter the beam centroid artificially. The "offset" values in the legend do not refer directly to the offset of the beam.

V_Q producing node at Q79	no. of oscillations	measured σ_0	calculated σ_0	
			$x_p \simeq 0$ mm	$x_p \simeq 7$ mm
5410	4.5	$43.8° \pm 0.6°$	$43.0°$	$43.2°$
5970	5.0	$48.6° \pm 0.6°$	$47.7°$	$48.0°$
6550	5.5	$53.5° \pm 0.6°$	$52.7°$	$52.9°$
7130	6.0	$58.4° \pm 0.6°$	$57.7°$	$58.0°$
7700	6.5	$63.2° \pm 0.6°$	$62.8°$	$63.1°$
8220	7.0	$68.1° \pm 0.6°$	$67.6°$	$67.9°$
8760	7.5	$73.0° \pm 0.6°$	$72.7°$	$73.0°$
9250	8.0	$77.8° \pm 0.6°$	$77.4°$	$77.8°$

Table 4.2: Comparison of values of σ_0 calculated from quadrupole voltage and particle energy with those from centroid measurements, using 122.5 keV Cs^+. The peak oscillation amplitude for the calculation of σ_0 is denoted by x_p.

matching calculations, using the radius and divergence values measured in the horizontal plane. Subsequent changes in quadrupole polarity did not exactly invert the x and y properties of the beam, so the beam was not precisely symmetric at the source.

First estimates of the required matching section configuration were calculated using a K-V envelope integration program written by L. J. Laslett and V. O. Brady. This program represents the quadrupole field by superposition of a Fourier-Bessel field expansion for each of the five matching quadrupoles and one of the periodic lenses. The expansion includes only the quadrupole, or $\cos(2\phi)$, terms with the associated Bessel function nonlinearities. The quadrupole focusing field is linearized during the integration by taking the effective gradient at each z position to be the ratio of the vacuum field calculated at the beam edge to the beam radius. The final tuning procedure used involved measuring the RMS beam radius in each transverse dimension in two consecutive quadrupole gaps, after M5 and Q1. The linear response

matrix calculated by varying four of the matching elements (usually M2–M5) in the envelope integration program provided a very dependable means of predicting corrected voltages. In most cases, five iterations were sufficient to provide a beam matched to within 10% envelope variation over the first 4 periods of periodic transport.

4.4 Emittance Measurements

Because we are using a double-slit emittance scanning method, only one point in the phase space distribution $f(x, x')$ can be determined per beam pulse. Hence pulse-to-pulse variation and overall reproducibility are important (discussed in section 7.8). In the early stages of the experiment, we had logged the data visually from the oscilloscope traces and moved the slits manually. This made the data analysis very tedious. The HP-85 system was therefore developed to handle the large number of data points (about 1000 per hour, with acquisition times of 1–1.5 hours). Almost all of the emittance data reported here are from the high-perveance, automated data acquisition mode.

4.5 Data Analysis

The RMS emittance is formally defined as

$$\epsilon_{\text{RMS}} \equiv \sqrt{\langle (x - \bar{x})^2 \rangle \langle (x' - \bar{x'})^2 \rangle - \langle (x - \bar{x})(x' - \bar{x'}) \rangle^2}. \qquad (4.1)$$

For a K-V beam, the RMS emittance is identically one-fourth of the actual emittance, and we have chosen to multiply the RMS emittance by this factor of 4 in calculating the emittance of our beam, following Lapostolle [14]:

$$\epsilon \equiv 4\epsilon_{\text{RMS}}. \qquad (4.2)$$

4.5.1 Stability Criterion

Our experimental procedure is straightforward. We set initial values for the current and emittance and measure the evolution of these parameters through the lattice. If the current and emittance are conserved throughout the lattice, we call the conditions "stable"; otherwise the conditions are called "unstable." This criterion has practical utility in the design of an accelerator for ICF work. The major purpose in identifying the boundary between "stability" and "instability" is to provide relevant information for the design of such accelerators.

4.5.2 Phase space data presentation

We present the phase space data in two graphic forms. First, we show the measured intensity contours in phase space, as in Fig. 5.2. These contours are measured at antisymmetry points along the channel, between lenses. At such points, the phase space contours (roughly elliptical in shape) are not upright, but are tilted with respect to the x and x' axes as a result of the convergence or divergence of the beam at the measurement point. In order to aid in viewing the contours, this tilt has been suppressed by a linear transformation of the x' axis, of the form $x' \rightarrow x' - ax$ in all plots of this type. The value for a is chosen to make the average value of the product of x with the new x' identically zero: $a = \langle xx' \rangle / \langle x^2 \rangle$. This is equivalent to translating the distribution to a symmetry point, except that the beam size retains the value for the antisymmetry point. In addition, we plot the emittance and current associated with the various intensity contours in the following way. We generate sub-distributions from the measured data by successively deleting points with values below certain thresholds in intensity. We then plot both the area occupied by the sub-distributions and the associated $\epsilon(i) = 4\epsilon_{\text{RMS}}(i)$ values against the partial current (i) represented by the sub-distributions, as

in Fig. 5.6. The area emittance is used only in these plots; the emittance from the RMS reduction is used everywhere else. Although the i vs. $\epsilon(i)$ curves do not reveal aberrations unless they are severe, the contour plots show them quite clearly.

4.5.3 Intensity parameterization and σ values

The emittance for the full beam current, $\epsilon(I)$, varies somewhat for the high-σ_0 measurements depending on how much "empty" phase space area surrounds the beam-occupied region, because of inclusion of noise in the data. The values for $\epsilon(0.95I)$ are more stable, and wherever values for the emittance are quoted, the value is for the 95% core of the beam distribution. This corresponds approximately to 90% of the beam when both dimensions are accounted for, assuming the distributions in the x and y planes are uncorrelated.

In our summary of maintainable beam intensity we must compare our results with the theoretical work, which has often been summarized in terms of the zero-current phase advance σ_0 and the space-charge "depressed" phase advance σ. We quantify the intensity of a beam by the value of σ derived for a K-V beam with the same current and emittance as measured for the non K-V beam, with the following justification. For a given σ_0, the parameter determining σ in the K-V treatment is ϵ/I. (This ratio does not uniquely specify non-K-V beam distributions, but if one scales a given beam distribution to different current, keeping the particle trajectories similar, the quantity ϵ/I remains constant. This same scaling can be inferred from Eqns. 2.5.) The nonlinear fields of a real beam with space-charge cause a spread in particle oscillation frequencies. However, because the forms of the K-V and RMS envelope equations are identical, the ratio of emittance to current determines the envelope stability for any beam for which the RMS equations are appli-

cable.

We derive values σ_{100} and σ_{95} as estimates for the average betatron frequencies of the beam particles using the linear theory in the following way. We use the emittance $\epsilon_{100} \equiv \epsilon(I)$ for the total beam current I, and also the emittance $\epsilon_{95} \equiv \epsilon(0.95I)$ for the most intense 95% of the beam current to derive depressed phase advance values σ_{100} and σ_{95}, respectively, for K-V beams with a ratio of emittance to current equal to ϵ_{100}/I and $\epsilon_{95}/0.95I$. We find that these two values are always close to each other, as shown in Fig. 5.11 and Table 5.1.